Optimal control of acoustic waves in solids

Young Sik Kim* and Herschel Rabitz
Department of Chemistry, Princeton University, Princeton, New Jersey 08544

Attila Askar
Mathematics Department, Bogazici University, Bebek-Istanbul, Turkey

John B. McManus
Aerodyne Research, Inc., Billerica, Massachusetts 01821-3976
(Received 29 October 1990)

Optimal dynamic normal surface loading of a homogeneous elastic solid for interior acoustic-energy focusing to a specific target volume is treated in this paper. The goal is achieved by additionally imposing the criteria of applying a relatively minimal total surface force and system disturbance except at the target. By utilizing the calculus of variations, the optimality conditions are obtained, and the approach is implemented through the finite-element method along with half-space dyadic Green's functions. The optimization procedure is done via the conjugate-gradient method. Numerical results show that the optimal normal surface loads consist of two radially shrinking concentric rings of special structure. For a positively constrained surface force, the earlier of the two surface load streams produces a self-focusing shear volume wave that moves to the target volume to create a high acoustic-energy density. An additional following longitudinal load adds further energy by compression of the surface directly over the target volume. In a second example without any positive constraint on the surface force, however, the earlier of the two surface load streams now produces a concentric surface wave as well as a self-focusing shear volume wave. An additional longitudinal load then converts the surface wave into bulk volume waves for achieving the objective with a minimum of total surface force and of total system disturbance. The overall approach of optimal design of dynamic surface loading for bulk volume objectives is flexible and capable of treating a variety of complex problems.

I. INTRODUCTION

There are a number of physical situations where it would be useful to produce a specified acoustic-wave structure within a solid, by applying a pattern of forces on the solid's surface. Here an acoustic wave refers to a vector elastic wave field and not just a scalar field as for sound waves in a fluid or air. The design of the optimum surface forcing to generate a specified wave is a complicated problem, especially if one takes into account technical or practical constraints. Optimal-control theory[1] is a branch of the calculus of variations that naturally takes into account the physical response, as well as practical constraints in calculating the optimum application of forces that move a physical system to a desired state. Optimal-control theory has been applied to a wide variety of problems in engineering science, especially for dynamical systems with many degrees of freedom and important constraints on the forces available to move the system. Recently, optimal-control theory has been used to calculate the optimum temporal structure of laser pulses for molecular site-specific photochemistry.[2] In the work presented here, we apply optimal-control theory to the systematic design of the moving forces on a solid surface for generating tailored acoustic-wave structures within a solid.

The generation of tailored electromagnetic (EM) waves has been studied since Brittingham's work,[3] which first suggested the possibility of a packetlike solution of Maxwell's equations. Such solutions are called focus wave modes (FWM's), which remain localized in three-dimensional space and move at the speed of light without dispersing. Unfortunately, a true FWM has an infinite total energy and is impossible to obtain. As a result of Brittingham's work, however, the possibility of solutions of the wave equation that are localized and slowly decaying in space-time has been reported by several groups. These include electromagnetic directed energy pulse trains,[4] acoustic directed energy pulse trains,[5] splash modes,[6] EM missiles,[7] Bessel beams,[8] EM bullets,[9] and transient beams.[10] These cases, with the exception of electromagnetic waves, are all for waves described as scalar fields. Within the author's knowledge such solutions for vector acoustic fields have not yet been treated. In the case of solid dynamics a proper physical description requires a vector field with longitudinal and shear waves traveling at different speeds. This apparent added complexity is in fact an attribute, as the vector field provides much greater ability for achieving the objective. In addition, it is natural to consider a free-half-space boundary problem for laboratory-realizable situations with solids. As a result one must use the half-space Green's functions that incorporate the more involved dynamics due to the free boundary. Thus, in this paper, it will be shown how

an optimal surface load can be designed to give a tailored acoustic vector field for a specific goal. The use of optimal control theory, in contrast to the other works mentioned above, allows for the inclusion of a broad family of ancillary criteria or practical constraints besides that of just achieving the original physical objective.

Acoustic waves have been long recognized as a valuable tool for studying and potentially manipulating the structure, dynamics and properties of solid materials.[11] A common problem for acoustic-wave studies is the process of generating or coupling the waves into the solid, which is made more difficult if one wants a specific wave characteristic, such as a focus. One approach to this problem is to act directly on the surface, rather than to use separate transducers, acoustic lenses,[12] and coupling media. Direct generation of acoustic waves at surfaces has been demonstrated using lasers[13,14] or electron beams[15] as well as with arrays of individually driven transducers.[16] The technique of laser acoustics is especially interesting from the perspective of the work presented here. Laser beams can be controlled both spatially and temporally, and energy can be delivered in a noncontacting manner in the ambient environment. Thus optimal-control techniques may be applied to the spatial and temporal design of laser pulses which act on a surface to generate tailored acoustic waves. The resultant tailored acoustic pulses could provide a new and possibly general tool for producing localized, strain fields in solids. We envision these acoustic wave forms and fields to be potentially useful in a broad range of applications for internal materials diagnostics and modifications.[17]

In the low strain linear medium regime the response of a solid to distributed surface forces can be described in terms of the superposition of responses due to point forces on the surface, with the response from each point source described by a dyadic Green's function. The acoustic response due to a single point force is fairly complex, with generated waves of shear, compressional, and surface modes, all of which have distinct spatial and angular dependence. If the solid is anisotropic, or nonlinear, then the response is even more complicated. If one desires to design the surface forces to produce a specific acoustic state in the interior of a solid, then it would be quite difficult to account for all of this complexity without a systematic procedure. Optimal-control theory provides a natural means to manage this complexity. In addition, optimal control theory allows one to include practical constraints as *cost functions,* in the calculation, so that one can, for example, derive the surface forcing function, which produces the best interior acoustic focus with the minimum expenditure of work in moving the surface.

We present here examples of optimal calculations of the moving forces on a solid surface, which produce a subsurface acoustic focus. In these examples, we assume a simplified physical situation that does not reflect a limitation in the general methodology. For the purposes of this paper, we treat the wave focus as a small volume with a desired maximum acoustic energy density, both kinetic and strain energy, without regard to the direction of local solid motion. There are other possible choices for defining a *focus* (e.g., maximum strain levels in a particular direction), the choice of which depends upon the specific application. We choose as cost functions the total disturbance of the system (except at the target time in the target volume) and the total surface loading, so that we may minimize the total energy of the system and the total surface force producing the focus. Again, there are other possible choices for the cost function, such as minimal laser energy required to drive the surface via opto-acoustic interactions[18] instead of the total surface loading. Here we treat the solid as an ideal isotropic elastic material, although anharmonic solids could be considered, and the optimization algorithm is of sufficient generality such that nonlinear materials could be treated as well. In the examples described in detail here, we consider bases both with and without a constraint that the surface forces be positive semidefinite.

In Sec. II of this paper, we formulate the optimal-control problem. The moving forces (control functions) are the surface loads, and the situation is identified as a boundary control problem. The objective of the control problem is to minimize a given objective functional, which depends on the state of the system (its displacement field) and its controls. The necessary optimality conditions for the problem are obtained from the variation of the objective functional with respect to the control functions. In Sec. III, we cast the problem in a discrete form, suitable for numerical solution. The state and costate equations are discretized on the surface [by the boundary element method (BEM)],[19] and in the target (focal) volume [by the finite element method (FEM)].[20] Next, the conjugate gradient algorithm[21] (CGA) of mathematical programming is used to minimize the derived objective functional of the optimal surface load control problem. In Sec. IV, we present numerical results for the optimum surface loads, shown as patterns that vary as a function of time and of radius from the center of symmetry defined by the target location. We also show a time sequence of the subsurface (bulk) acoustic-energy density. The reformulation of the dyadic Green's functions for a symmetric ring-type load[22] is presented in the Appendix.

II. OPTIMAL-CONTROL PROBLEM

Consider an elastic, homogeneous and isotropic half space whose free surface is subjected to a dimensionless boundary traction $\tau(\mathbf{x},t)$. Using the dimensionless displacement field $\mathbf{u}(\mathbf{x},t)$ as the state function, the system equations in the domain V with its boundary S may be written in dimensionless form as

$$\mu\nabla^2\mathbf{u}+(\lambda+\mu)\nabla\nabla\cdot\mathbf{u}=\rho\frac{\partial^2}{\partial t^2}\mathbf{u}, \quad (\mathbf{x},t)\in V\times T^+ . \quad (1)$$

Here, the dimensionless displacements, surface tractions, energy density, Lamé's constants, mass density, coordinates, time, and Green's functions are defined in terms of their dimensional counterparts by

$$\mathbf{u}=\hat{\mathbf{u}}/Z_0;\quad \tau=\hat{\tau}/\hat{\rho}c_d^2;\quad \epsilon=\hat{\epsilon}/\hat{\rho}c_d^2\ ,$$
$$\lambda=\hat{\lambda}/\hat{\rho}c_d^2;\quad \mu=\hat{\mu}/\hat{\rho}c_d^2;\quad \rho=\hat{\rho}/\hat{\rho}=1\ , \tag{2}$$
$$\mathbf{x}=\hat{\mathbf{x}}/Z_0;\quad t=c_d\hat{t}/Z_0;\quad \mathbf{G}=\hat{\rho}c_d Z_0^2\hat{\mathbf{G}}\ .$$

The longitudinal and shear wave velocity c_d and c_s are defined by $c_d^2=(\hat{\lambda}+2\hat{\mu})/\hat{\rho}$ and $c_s^2=\hat{\mu}/\hat{\rho}$, respectively, and Z_0 is some characteristic length, and the hat symbol is used to denote the corresponding dimensional variable. After this point, unless otherwise stated, all quantities are in dimensionless form.

For convenience, the standard index notation has been adopted where summation is assumed over repeated indices, commas with following indices denote spatial differentiation, and dots indicate differentiation with respect to time t.[11] Within this section, unless otherwise states, $u_i=u_i(\mathbf{x},t)$, $\tau_i=\tau_i(\mathbf{x},t)$, and $\psi_i=\psi_i(\mathbf{x},t)$. Then, Eq. (1) can be rewritten as

$$\mu u_{i,jj}+(\lambda+\mu)u_{j,ji}=\rho\ddot{u}_i,\quad (\mathbf{x},t)\in V\times T^+\ . \tag{1'}$$

The initial and boundary conditions are

$$u_i(\mathbf{x},0)=\dot{u}_i(\mathbf{x},0)=0,\quad \mathbf{x}\in V\ , \tag{3a}$$

$$\lambda u_{j,j}n_i+\mu(u_{i,j}+u_{j,i})n_j=\tau_i,\quad (\mathbf{x},t)\in S\times T^+\ , \tag{3b}$$

where n_i are the direction cosines of the unit vector normal to the surface S.

Using the half-space dyadic Green's functions $G_{ij}^{(+)}$, one may obtain $u_i(\mathbf{x},t)$ at any point in the half space as[23]

$$u_i(\mathbf{x},t)=\rho\int_V dV\left[G_{ij}^{(+)}\frac{\partial}{\partial t_0}u_j(\mathbf{x}_0,t_0)-u_j(\mathbf{x}_0,t_0)\frac{\partial}{\partial t_0}G_{ij}^{(+)}\right]_{t_0=0}+\int_0^t dt_0\int_S dS\,G_{ij}^{(+)}\tau_j(\mathbf{x}_0,t_0)\ . \tag{4}$$

From the initial conditions in Eq. (3), Eq. (4) can be reduced to a boundary integral equation.

In the present optimization problem, it is desired to maximize acoustic energy in a local subsurface target volume at a particular time in an efficient manner such that the total energy of the system remains as small as possible elsewhere and by applying a minimum surface force by means of the controllable surface traction during the process. Thus, the physical objective functional may be written as

$$J[u_i,\tau_i]=\Phi(T)+L\ , \tag{5}$$

with

$$\Phi(T)=\left|\int_{V_c}dV\,\epsilon(\mathbf{x},T)-E_p\right|\ , \tag{6}$$

$$L_1=w_1\left[\int_V dV\int_0^T dt\,\epsilon(\mathbf{x},t)-w_1'\int_{V_c}dV\,\epsilon(\mathbf{x},T)\right]\ , \tag{7a}$$

$$L_2=\frac{w_2}{2}\int_s dS\int_0^T dt\,\tau_i^2\ , \tag{7b}$$

where the error function $\Phi(T)$ measures the degree of satisfaction of the objective of localizing the energy in the local target volume V_c at the target time $t=T$ at a specified value E_p. In competition with this goal are the penalty cost functions $L=L_1+L_2$, respectively corresponding to the desire for minimizing the total energy of the system except in the volume V_c at $t=T$ and the total surface force during the energy focusing process. The total energy density $\epsilon(\mathbf{x},t)$ may be expressed as a sum of the kinetic energy density $k(\mathbf{x},t)$ and strain energy density $s(\mathbf{x},t)$ as

$$\epsilon(\mathbf{x},t)=k(\mathbf{x},t)+s(\mathbf{x},t)$$
$$=\frac{\rho}{2}\dot{u}_i\dot{u}_i+\frac{\lambda}{2}(u_{k,k})^2+\frac{\mu}{2}u_{i,j}(u_{i,j}+u_{j,i})\ . \tag{8}$$

The choice of the weight factors w allows for flexibility in balancing the role of the Φ and L contributions to J. The choice of weights is a standard practical issue in applied optimal-control theory.[21] The numerical computations in Sec. IV will illustrate some of the logic involved with specific results for different choices for w.

The dynamic optimization of surface loading for the purpose of efficient focusing of acoustic energy within the solid interior may be stated as the problem of finding the optimal control function τ_i from a set of admissible controls such that the objective functional J is minimized under the system constraints Eqs. (1) and (3). It is well known that a constrained minimization problem can be treated as an unconstrained one by introducing Lagrange multiplier functions (ψ_i);[21] that is, instead of minimizing J with constraints Eqs. (1) and (3), one can minimize the modified objective functional

$$\bar{J}[u_i,\tau_i,\psi_i]=J-\int_V dV\int_0^T dt\,\psi_i[\mu u_{i,jj}+(\lambda+\mu)u_{j,ji}-\rho\ddot{u}_i]\ . \tag{9}$$

The necessary condition for $\bar{J}$ to be stationary is that

$$\delta\bar{J}[u_i,\tau_i,\psi_i]=\delta J+\delta M$$
$$=\delta\Phi(T)+\delta L_1+\delta L_2+\delta M=0\ , \tag{10}$$

where M refers to the new integral term in Eq. (9). By utilizing the following variational equations with the system constraints, Eqs. (1) and (3),

$$\int_V dV\,\delta k=\int_V dV\,\rho\dot{u}_i\delta\dot{u}_i\ , \tag{11}$$

$$\begin{aligned}\int_V dV\,\delta s&=\int_V dV\{[\mu u_{i,jj}+(\lambda+\mu)u_{j,ji}-\rho\ddot{u}_i]\delta u_i+\lambda u_{k,k}\delta u_{k,k}+\mu(u_{i,j}+u_{j,i})\delta u_{i,j}\}\\&=\int_V dV\{\lambda(u_{j,j}\delta u_i)_{,i}+\mu[(u_{i,j}+u_{j,i})\delta u_i]_{,j}-\rho\ddot{u}_i\delta u_i\}\\&=\int_S dS[\lambda u_{j,j}n_i+\mu(u_{i,j}+u_{j,i})n_j]\delta u_i-\int_V dV\,\rho\ddot{u}_i\delta u_i\\&=\int_S dS\,\tau_i\delta u_i-\int_V dV\,\rho\ddot{u}_i\delta u_i\ ,\end{aligned} \tag{12}$$

and recognizing that the total energy of the system at time t is equal to the sum of the power input from time 0 to t,

$$\int_V dV\epsilon(\mathbf{x},t)=\int_S dS\int_0^t d\nu\,\tau_i(\mathbf{x},\nu)\dot{u}_i(\mathbf{x},\nu)\ , \tag{13}$$

we can write $\delta\Phi(T)$, δL_1, δL_2, and δM as

$$\delta\Phi(T)=\mp\left[\int_{V_c}dV\,\rho[\dot{u}_i(\mathbf{x},T)\delta\dot{u}_i(\mathbf{x},T)-\ddot{u}_i(\mathbf{x},T)\delta u_i(\mathbf{x},T)]+\int_{S_c}dS\,\tau_i(\mathbf{x},T)\delta u_i(\mathbf{x},T)\right]\ , \tag{14}$$

$$\begin{aligned}\delta L_1=&w_1\int_S dS\int_0^T dt\int_0^t d\nu\{[\dot{u}_i(\mathbf{x},\nu)\delta\tau_i(\mathbf{x},\nu)-\dot{\tau}_i(\mathbf{x},\nu)\delta u_i(\mathbf{x},\nu)]+\tau_i\delta u_i\}\\&-w_1w_1'\left[\int_{V_c}dV\,\rho[\dot{u}_i(\mathbf{x},T)\delta\dot{u}_i(\mathbf{x},T)-\ddot{u}_i(\mathbf{x},T)\delta u_i(\mathbf{x},T)]+\int_{S_c}dS\,\tau_i(\mathbf{x},T)\delta u_i(\mathbf{x},T)\right]\ ,\end{aligned} \tag{15}$$

$$\delta L_2=w_2\int_S dS\int_0^T dt\,\tau_i\delta\tau_i\ , \tag{16}$$

$$\delta M=-\int_V dV\int_0^T dt\{[\mu u_{i,jj}+(\lambda+\mu)u_{j,ji}-\rho\ddot{u}_i]\delta\psi_i+\psi_i[\mu\delta u_{i,jj}+(\lambda+\mu)\delta u_{j,ji}-\rho\delta\ddot{u}_i]\}\ , \tag{17}$$

where the $-$ sign in Eq. (14) is operative when the energy in the target volume V_c at $t=T$ is less than a specific value E_p and *vice versa* for the $+$ sign. By using the following identities[24] with the initial condition in Eq. (3),

$$\psi_i\delta u_{j,ji}=(\psi_i\delta u_{j,j})_{,i}-(\psi_{,i}\delta u_j)_{,j}+\psi_{i,ij}\delta u_j\ , \tag{18}$$

$$\psi_i(\delta u_{i,jj}+\delta u_{j,ij})=[\psi_i(\delta u_{i,j}+\delta u_{j,i})]_{,j}-(\psi_{i,j}\delta u_i)_{,j}-\psi_{i,jj}\delta u_i+(\psi_{i,j}\delta u_j)_{,i}-\psi_{i,ij}\delta u_j\ , \tag{19}$$

and

$$\int_0^T dt\,\psi_i\delta\ddot{u}_i=\psi_i\delta\dot{u}_i|_0^T-\int_0^T dt\,\dot{\psi}_i\delta\dot{u}_i=\psi_i(\mathbf{x},T)\delta\dot{u}_i(\mathbf{x},T)-\dot{\psi}_i(\mathbf{x},T)\delta u_i(\mathbf{x},T)+\int_0^T dt\,\ddot{\psi}_i\delta u_i\ , \tag{20}$$

then Eq. (17) can be rewritten as

$$\begin{aligned}\delta M=&-\int_V dV\int_0^T dt\{[\mu u_{i,jj}+(\lambda+\mu)u_{j,ji}-\rho\ddot{u}_i]\delta\psi_i+[\mu\psi_{i,jj}+(\lambda+\mu)\psi_{j,ji}-\rho\ddot{\psi}_i]\delta u_i\}\\&-\int_S dS\int_0^T dt\{\psi_i[\lambda\delta u_{j,j}n_i+\mu(\delta u_{i,j}+\delta u_{j,i})n_j]-[\lambda\psi_{j,j}n_i+\mu(\psi_{i,j}+\psi_{j,i})n_j]\delta u_i\}\\&+\int_V dV\,\rho[\psi_i(\mathbf{x},T)\delta\dot{u}_i(\mathbf{x},T)-\dot{\psi}_i(\mathbf{x},T)\delta u_i(\mathbf{x},T)]\ .\end{aligned} \tag{21}$$

Substituting Eqs. (14)–(16) and (21) into Eq. (10), the stationary condition for $\bar{J}$ may be derived from the fact that the variations δu_i, $\delta\tau_i$, and $\delta\psi_i$ are independent of each other; hence, their coefficients can be set equal to zero, separately. Thus, the costate (the Lagrange multiplier) equations of motion can be written as

$$\mu\psi_{i,jj}+(\lambda+\mu)\psi_{j,ji}=\rho\ddot{\psi}_i,\quad(\mathbf{x},t)\in V\times T^+\ , \tag{22}$$

where the costate boundary condition and final conditions at $t=T$ are, respectively,

$$\lambda\psi_{j,j}n_i+\mu(\psi_{i,j}+\psi_{j,i})n_j=\tau_i^c,\quad(\mathbf{x},t)\in S\times T^+\ , \tag{23}$$

$$\tau_i^c=w_1[(T-t)\dot{\tau}_i-\tau_i]\ , \tag{24}$$

$$\psi_i(\mathbf{x},T)=\begin{cases}(w_1w_1'\pm1)\dot{u}_i(\mathbf{x},T)\\0\end{cases},\quad\dot{\psi}_i(\mathbf{x},T)=\begin{cases}(w_1w_1'\pm1)\ddot{u}_i(\mathbf{x},t),&\text{if }\mathbf{x}\in V_c\ ,\\0,&\text{otherwise}\ ,\end{cases} \tag{25}$$

where τ_i^c denotes the costate boundary traction. Note that the equation of motion for the costate function ψ_i is the same as that of the displacement field. This is a consequence of the self-adjointness of the wave operator.

The gradient of $\bar{J}$ with respect to the control functions τ_i can be written as

$$\frac{\delta \bar{J}}{\delta \tau_i(r,t)} = \int_S dS(\gamma_0) \int_0^T dt_0 \left[w_1 \int_0^{t_0} d\nu\, \dot{u}_i(\gamma_0,\nu)\delta(\gamma-\gamma_0)\delta(t-\nu) + [w_2\tau_i(\gamma_0,t_0) - \psi_i(\gamma_0,t_0)]\delta(\gamma-\gamma_0)\delta(t-t_0) \right]$$
$$= 2\pi r[w_1 \int_0^T dt_0 \dot{u}_i(\gamma,t)h(t_0-t) + w_2\tau_i - \psi_i]$$
$$= 2\pi r[w_1(T-t)\dot{u}_i + w_2\tau_i - \psi_i], \quad (\gamma,t)\in S\times T^+ , \tag{26}$$

where $h(t)$ is the unit step function and this gradient will be utilized in the iteration procedure for finding the optimal function τ_i.

The costate function can be written as follows in terms of the half-space dyadic Green's function:

$$\psi_i(\mathbf{x},t) = \rho \int_V dV \left[G_{ij}^{(-)} \frac{\partial}{\partial t_0} \psi_j(\mathbf{x}_0,t_0) - \psi_j(\mathbf{x}_0,t_0) \frac{\partial}{\partial t_0} G_{ij}^{(-)} \right]_{t_0=T} + \int_T^t dt_0 \int_S dS\, G_{ij}^{(-)} \tau_j^c(\mathbf{x}_0,t_0) , \tag{27}$$

where the advanced dyadic Green's function $G_{ij}^{(-)}(\mathbf{x},t;\mathbf{x}_0,t_0)$ describes the ith directional effect at $\mathbf{x}$ corresponding to a jth directional unit impulse at $\mathbf{x}_0$ with, however, the sense of time reversed, so that the event at t occurs at some time *earlier* that the impulse causing it at a time t_0 (i.e., $t<t_0$). Thus, from the reciprocal relation the advanced dyadic Green's function can be rewritten as[25]

$$G_{ij}^{(-)}(\mathbf{x},t;\mathbf{x}_0,t_0) = G_{ij}^{(+)}(\mathbf{x},-t;\mathbf{x}_0,-t_0)$$
$$= G_{ij}^{(+)}(\mathbf{x},t_0;\mathbf{x}_0,t) . \tag{28}$$

Until now, we have allowed the optimal surface loads to take on both positive and negative values. However, in the laboratory, it is quite difficult to generate negative surface loads with optical means (other techniques could achieve such negative forces by first uniformly preloading the surface and selectively relaxing the force). Thus, we may desire to constrain the surface load to assume only positive values. For this constraint, we define the surface traction τ_i as follows, so that we can have only positive surface load P_i,

$$\tau_i(r,t) = -P_i(r,t) = -\frac{p_i^2(r,t)}{2} , \tag{29}$$

and the positive constrained optimal problem can be reformulated with new cost function L_2 as

$$L_2 = \frac{\omega_2}{2} \int_S dS \int_0^T dt\, p_i^2 . \tag{30}$$

From the same procedure, one finds the same costate constraints except the gradient equation is now

$$\frac{\delta \bar{J}}{\delta p_i} = -w_1(T-t)\dot{u}_i p_i + w_2 p_i + \psi_i p_i, \quad (\mathbf{x},t)\in S\times T^+ . \tag{31}$$

The optimization problem is reduced to solving the state function [Eq. (4)] and the costate function [Eq. (27)] integral equation iteratively in the direction of minimizing the objective functional J until a specified convergence criteria are satisfied. In other words, by taking an initial guess for τ_i on S, the state problem may be solved for u_i from Eq. (4) with Eq. (3). With this u_i, the costate problem Eq. (27) may consequently be solved for ψ_i with Eqs. (23)–(25). Better values for the control function τ_i can be found via the CGA (Ref. 21) by using the objective functional J [Eq. (5)] and its gradient with respect to τ_i [Eq. (26) or (31)].

III. NUMERICAL PROCEDURE

The continuous space-time optimal-control problem posed above can be rendered to a mathematical-programming (MP) problem of minimizing a functional over a set of coefficients subject to algebraic constraints. In order to apply a MP technique directly to the optimal control problem, the continuous space-time system of Eqs. (4) and (27) have to be discretized in space and time. However, using the half-space dyadic Green's function the optimal control theory avoids requiring a discretization of the whole space domain. The discretization of the boundary surface and target volume is enough to apply the MP technique. For this purpose the boundary surface is discretized as a series of axial-symmetric ring segments by the BEM and the target volume (V_c) will be discretized as a series of cylindrical segments by the FEM. Within the present constraint of axial symmetry, any target volume shapes could be considered. The choice of cylindrical symmetry is the natural choice here in keeping with the uniform nature of the solid and the symmetry of the target volume. The remainder of this section will give a concise summary of our numerical procedures, which are based on reliable existing methods.[19–21] The algorithm was successfully tested on several standard acoustic propagation problems and was found to be quite accurate.

Special care should be taken on the choice of time intervals and boundary discretization in order to avoid violating the causality property of the Green's function;[25] that is, in a time step, the spatial nodes should not communicate and should be localized. Thus, the parameter α, given by $\alpha = c_d \Delta\hat{t}/\Delta\hat{r} = \Delta t/\Delta r$, should be chosen $\alpha < 1$. Here Δr and Δt are the dimensionless grid spacing and time increment.

In keeping with the presently assumed system axial symmetry, the surface traction need only be discretized on radial nodal points. Taking into account the axial symmetry of the system and the restriction that the surface traction be perpendicular to the surface, the surface traction $\tau_z(r,t)$, displacements $u_i(r,z,t)$, and costate

function $\psi_z(r,t)$ can be approximated to $\tau_z^*(r,t)$, $u_i^*(r,z,t)$, and $\psi_z^*(r,t)$ through interpolation functions as

$$\tau_z^*(r,t)=\sum_j\sum_n \phi^n(t)\eta^j(r)\tau_z^{n,j} , \tag{32}$$

$$u_i^*(r,z,t)=\sum_j\sum_n\sum_l \theta^n(t)\eta^j(r)h^l(z)u_i^{n,j,l} , \tag{33}$$

$$\psi_z^*(r,t)=\sum_j\sum_n \phi^n(t)\eta^j(r)\psi_z^{n,j} , \tag{34}$$

where j, l, and n refer to radius, depth, and time discretization point indices. The expansion coefficients are intended to represent the boundary values through the conditions

$$\begin{aligned}&\phi^m(t_n)=\theta^m(t_n)=\delta_{mn} ,\\ &\eta^j(r_k)=\delta_{jk} ,\\ &h^l(z_m)=\delta_{lm} .\end{aligned} \tag{35}$$

Since the displacement in Eq. (4) is related to a time integral of the surface tractions, if we choose piecewise constant time interpolation functions for $\phi^n(t)$ in the traction, then a suitable type of time interpolation for the displacement $\theta_n(t)$ is a piecewise linear function

$$\phi^n(t)=\begin{cases}1, & \text{if } t_n\geq t\geq t_{n-1}\\ 0, & \text{otherwise} .\end{cases} \tag{36}$$

$$\theta^n(t)=\begin{cases}1-|t-t_n|/\Delta t, & \text{if } t_{n+1}\geq t\geq t_{n-1}\\ 0, & \text{otherwise} .\end{cases} \tag{37}$$

Substitution of τ_z^* and u_i^* for τ_z and u_i in Eq. (4) yields a system of algebraic equations

$$\begin{aligned}u_i^{n,j,l}&=\sum_k\sum_{m=1}^{n} G_{R,iz}^{nm,jk,l}\tau_z^{m,k}\\ &=\sum_k\sum_{m=0}^{n-1} G_{R,iz}^{m,jk,l}\tau_z^{(n-m),k} ,\end{aligned} \tag{38}$$

where

$$\begin{aligned}G_{R,iz}^{m,jk,l}=2\pi&\int_{r_{k-1}}^{r_{k+1}} dr_0 r_0\eta^k(r_0)\\ &\times\int_{t_m}^{t_{m+1}} dt_0 G_{R,iz}(r_j,z_l,t_0;r_0) .\end{aligned} \tag{39}$$

The dyadic ring Green's function $G_{R,iz}(r_j,z_l,t_m;r_0)$ denotes the effect in the ith direction at the receiver (r_j,z_l,t_m) due to a z-directional ring impulse load,

$$\tau_z(r,t)=\frac{-1}{2\pi r}\delta(r-r_0)\delta(t) ,$$

at r_0. The dyadic ring Green's function is very useful for the present case of an axially symmetric system and may be derived from the impulse point-load Green's function (see the Appendix). The radial integration in Eq. (39) is carried out numerically using Gauss quadrature formulas for all time steps so one can avoid the singular behavior when the distance between the receiver and source tend to zero. Due to the choice of time interpolation in Eq. (36), the time derivative of Eq. (38) can be written in finite difference form as

$$\dot{u}_i^{n,j,l}=(u_i^{n+1,j,l}-u_i^{n-1,j,l})/2\Delta t . \tag{40}$$

Similarly, Eq. (27) can be approximated by Eqs. (32)–(34) as

$$\begin{aligned}\psi_z^{n,j}=\pm\rho&\sum_k\sum_l (G_{Q,zi}^{N-n,jk,l}\ddot{u}_i^{N,k,l}-\dot{G}_{Q,zi}^{N-n,jk,l}\dot{u}_i^{N,k,l})\\ &+\sum_k\sum_{m=0}^{N-n} G_{R,zz}^{m,jk,0}\tau_z^{c(m+n),k} ,\end{aligned} \tag{41}$$

where the target time is $T=t_N$ and

$$\begin{aligned}G_{Q,zi}^{N-n,jk,l}=2\pi&\int_{r_{k-1}}^{r_{k+1}} dr_0 r_0\eta^k(r_0)\\ &\times\int_{z_{l-1}}^{z_{l+1}} dz_0 h_l(z_0)\\ &\times G_{R,zi}(r_j,t_{N-n};r_0,z_0) .\end{aligned} \tag{42}$$

Here, the reciprocal relation for the Green's function has been used for the dyadic ring Green's function as

$$G_{R,zi}(r_j,t_{N-n};r_0,z_0)=G_{R,iz}(r_0,z_0,t_{N-n};r_j) . \tag{43}$$

Through this procedure by assuming an initial value for the control function $\tau_z^{n,j}$ on the surface, the discrete values of the state function $u_i^{n,j,l}$ in the target volume V_c are uniquely determined by direct time integration using the BEM [Eq. (38)]. The corresponding discrete values of the costate function $\psi_z^{n,j}$ on the surface may be found by backward time integration using the FEM [Eq. (41)]. From these values, one can calculate the objective functional and its gradient with respect to the control function. Then, from the CGA, one may calculate the direction of search from past and present values of the objective and its gradient. Better values of the discrete control function $\tau_z^{n,j}$ for the next iteration step are determined by a one-dimensional minimization along the direction of search, which is always the direction of descent. Thus, the algorithm tends to converge, and the iteration procedure is repeated until the sum of squares of the components of the gradient vector is less than a specified tolerance. A standard library routine has been utilized for the CGA optimization.[26]

IV. NUMERICAL RESULTS AND DISCUSSIONS

In this section we shall show how the algorithm developed above can be used to design optimal dynamic normal surface loads for achieving efficient subsurface acoustic-energy focusing. We have based the calculations upon the physical properties of an aluminum alloy for concreteness and the relevant physical properties[27] of Al 2024 are the mass density $\hat{\rho}=2.77$ g/cm^3, and Lamé constants $\hat{\lambda}=0.546$ g/cm μs^2, $\hat{\mu}=0.257$ g/cm μs^2. The longitudinal and shear wave velocity are, respectively, $c_d=0.618$ cm/μs and $c_s=0.304$ cm/μs. The objective of the problem is to find the temporally and spatially optimized normal load that achieves as nearly as possible the local energy E_p in V_c below the surface at $t=T$ by apply-

ing relatively minimal surface forces, while generating as little possible system disturbance elsewhere.

For this axial-symmetric problem depicted in Fig. 1, we assume the maximum radius of the surface load to be $R_0/Z_0=2.5$, which is divided into 25 axial-symmetric ring segments with $\Delta r=0.1$. Similarly, the depth from the surface z is discretized with the same mesh refinement $\Delta z=0.1$. The target volume V_c is a cylinder of radius $r=0.2$ and height 0.4 centered at $z_c=0.8$, which was discretized as eight axial-symmetric ring elements, and each element has nine nodal points. P_z stands for the optimal normal surface loading, which is related to surface traction τ_z as $P_z=-\tau_z$ at $z=0$. Also, the target time is taken as $T=7.0$ in order to allow sufficient time for all possible control mechanisms to act. In order to preserve the causality property of the Green's function, a time step $\Delta t=0.046$ was adopted.

A. Control with a positive load constraint

First, we demonstrate the design of an optimal dynamic normal load, which is allowed to take on only positive values. Starting with the initial guess of 25 axial-symmetric ring loads for each time step, the vertical and radial displacement fields in the target volume can be calculated from Eq. (4). With these displacement fields, the normal costate field on the surface may consequently be solved by Eq. (27). Finally, the displacement fields, the costate field, and the initially guessed surface load are used to calculate the objective functional J and its gradient vector. By using the CGA, one can find a better value of the surface load for the next iteration. Here, we chose equally small, but not negligible, ring loads for all time and space as an initial guess. For the convergence criteria, the iteration procedure is repeated until the sum of squares of the gradient components is less than a specified tolerance 10^{-9}.

We have performed three different numerical calculations for this case to study the characteristics of the optimal surface normal loads depending on the weights of the cost functions. Figure 2(a) shows the positive constrained optimal surface normal load as a function of time and radius for the case $w_1=0$ and $w_2=1.0$, so that the acoustic energy will be focused in the target volume by applying only minimal surface force. The corresponding time sequence of the optimally controlled energy density contour plots inside the solid (same domain as Fig. 1) are shown in Fig. 2(b). It is seen that the optimal normal load mainly consists of two shrinking concentric normal ring loads. From now on, we call the earlier concentric loading stream P_s and the later stream P_d. The P_s and

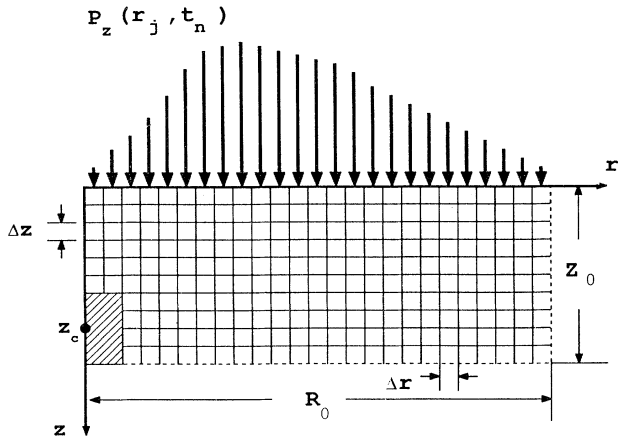

FIG. 1. Finite-element mesh for the half space under the axial-symmetric surface load $P_z(r,t)$. The shaded part denotes the target volume V_c, which is centered at $(r,z)=(0.0,0.8)$.

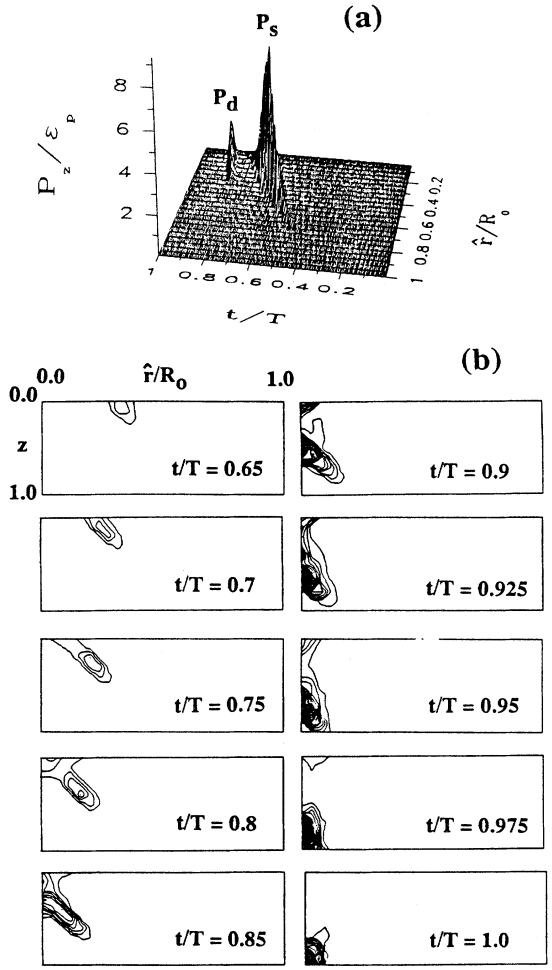

FIG. 2. (a) The positive constrained optimal surface normal load and (b) the corresponding time sequence of optimally controlled energy density contour maps inside the Al alloy for the weights $w_1=0.0$ and $w_2=1.0$. The contour interval is $\Delta\epsilon/\epsilon_p=0.5$, where the target energy density is defined as $\epsilon_p=E_p/V_c$ and the target time is $t/T=1$. Note that by applying only minimal surface force most of the focused acoustic energy is generated by the shear motions with constructive interference and the maximal energy concentration occurring before the target time.

P_d streams shrink to the center of the surface with the velocity v_s and v_d, respectively, and the P_d load is concentrated directly above the target volume, while the P_s load stream has a maximum load value at $r \sim 0.34$. Also, the maximum value of the P_s load is about four times larger than that of the P_d load.

In order to explain the characteristics of the optimal load streams, we have calculated the concentric ring loads whose shear and longitudinal wave fronts arrive at the center of the target at the time T with the velocity of the shear wave c_s and of longitudinal wave c_d, respectively (i.e., neglecting the target volume size). For this purpose, the loads at radius r satisfy equations $c_d(T-t)=(r^2+z_c^2)^{1/2}$ for the P_d load stream and $c_s(T-t)=(r^2+z_c^2)^{1/2}$ for the P_s load stream. Thus, for the waves transmitted from different points to reach the target center at the same time, the load stream velocities for P_d and P_s are obtained as $v_d(r)=-c_d(r^2+z_c^2)^{1/2}/r$ and $v_s(r)=-c_s(r^2+z_c^2)^{1/2}/r$ by differentiating the above equations, respectively. Figure 3 shows the contour plot of Fig. 2(a) and the predicted r versus t load stream relations whose velocities are v_d and v_s. It is seen that velocities of the optimal surface load streams and of the predicted load streams are quite well fitted by the velocity calculations except for a small shift due to the target volume size. Thus, it has been demonstrated that by applying minimal surface force the optimal load streams P_d and P_s with velocities v_d and v_s may achieve an efficient subsurface acoustic-energy focusing by transmitting mostly longitudinal and shear motions with *constructive interference* to produce a superposition of both waves in phase in the target volume at the target time.

The qualitative radial variation of the optimal surface load and the proportion of the longitudinal to the shear wave contribution may also be predicted from the theoretical acoustic radiation pattern for the steady-state fields.[28] The Fourier transforms of wave front discontinuities in the transient dyadic Green's functions have the same amplitude as the steady-state solutions, so that these discontinuities contribute with the same intensity to the radiation energy. Figure 4 shows the mean intensities of the longitudinal and shear waves at the center of the target volume produced by steady-state unit ring loads at the different radii. It is seen that the radial variation and the proportion of the longitudinal to the shear wave contribution are in good qualitative agreement with the optimal surface load in Fig. 2(a) except for the dip in the shear wave at $r \sim 0.2$, which would be lost taking into account the finite size of the target volume. Also, we see that at the target time, almost all of the acoustic energy is localized in the target volume, however, the maximal energy density occurs before the target time (at $t/T=0.925$). Because of the occurrence of high-energy density before the target time due to the choice of the cost function, the yield of the controlled energy focusing is just 13%. This figure means that only 13% of the energy input to the surface can be controlled to be focused into the target volume at the target time.

Figures 5(a) and 5(b) show the same case except for the $w_1=0.32$ and $w_2=0.0$, so that the objective has been achieved with only the minimum system disturbance. Here, the weight factor w_1' in Eq. (7a) was chosen as the time step Δt. Most of energy is transmitted from the P_d load stream near the center of the surface as compressional motion [note that the contour interval in Fig. 5(b) is different from that in Fig. 2(b)]. Apparently this is the

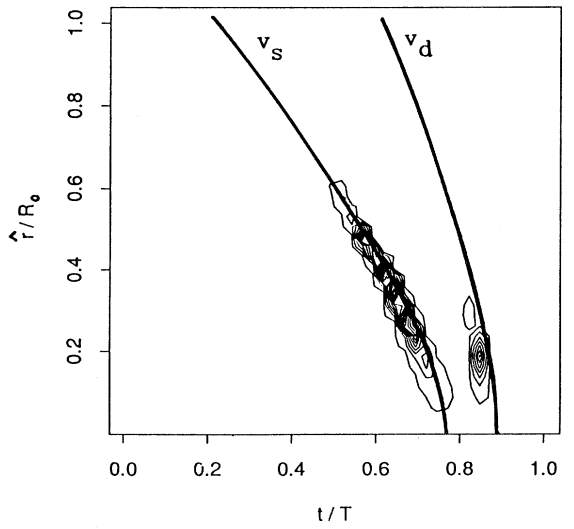

FIG. 3. The contour plot of the positive constrained optimal surface load in Fig. 2(a) and the predicted load r vs t relations that transmit the waves to the target center at the target time with the respective velocities c_d and c_s. The corresponding velocities v_d and v_s are obtained by the slope dr/dt. It is evident that the P_d and P_s load streams transmit mostly corresponding longitudinal and shear motions.

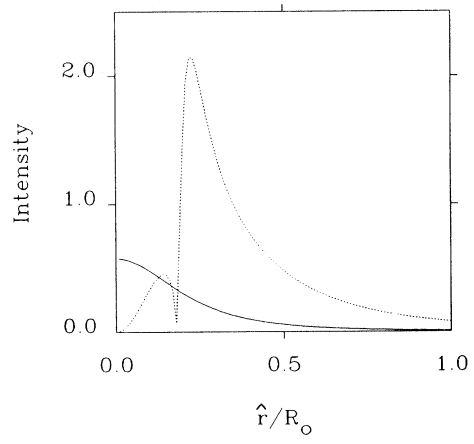

FIG. 4. The mean intensities of the longitudinal and shear waves at the center of the target volume produced by the steady-state unit ring loads as a function of radius from $r=0$ to 1. The solid curve is for the longitudinal wave, while the dashed curve is for the shear wave. It shows good qualitative agreement with the optimal surface load in Fig. 2(a) except for the dip in the shear wave at $r \sim 0.2$, which may be ascribed to taking into account the target volume size.

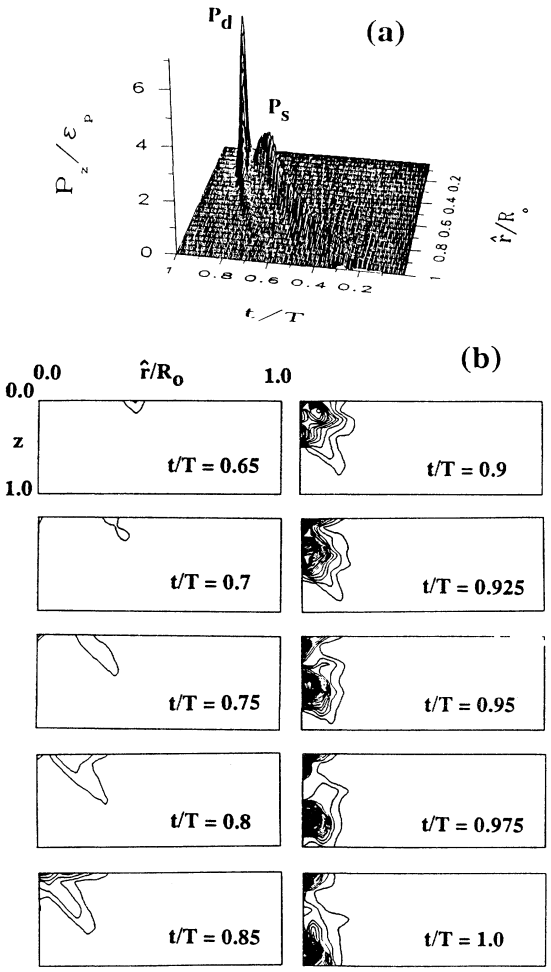

FIG. 5. Same as Fig. 2 except for $w_1=0.32$ and $w_2=0.0$. The contour interval is 0.1. Note that with only the minimum system disturbance, most of focused acoustic energy is generated by the longitudinal motions due to the highly concentrated surface load near the center of the surface.

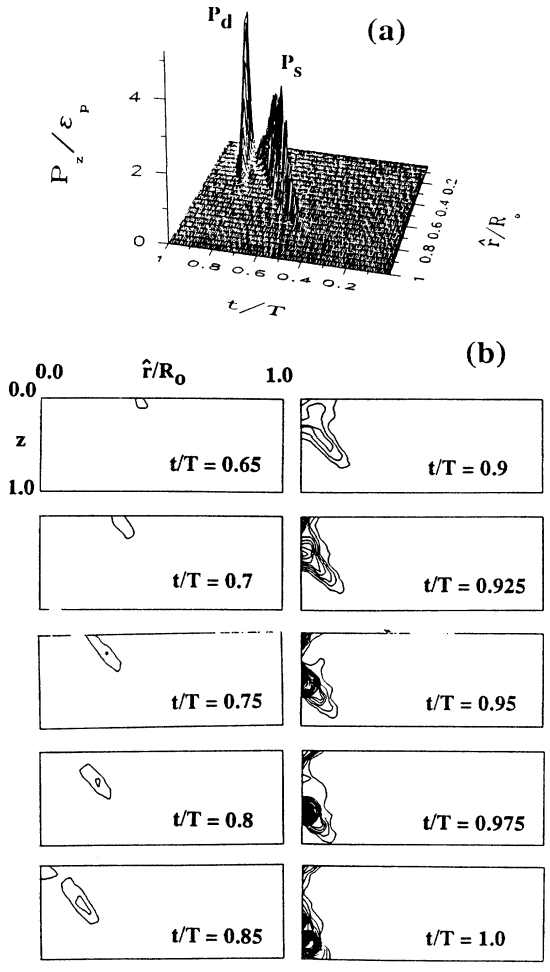

FIG. 6. Same as Fig. 2 except for $w_1=0.21$ and $w_2=0.6$. The contour interval is 0.3. Note that by applying a surface force as small as possible with relatively small system disturbance, the objective is achieved by well balanced shear and longitudinal motion in order to avoid an early maximum energy occurrence and a localized high surface load.

most efficient way to transmit the acoustic energy to the target volume at the target time with minimal system disturbance elsewhere. The small P_s load stream creates a surface wave that will eventually be converted into a bulk volume wave by the P_d load stream to better achieve the objective. The origin of these conclusions will be discussed in detail later. Again, at the target time $t=T$, most of the acoustic energy is localized in the target volume, and furthermore the maximum energy density occurs at the target time. Thus, the yield of this case is an efficient 65%. However, a high surface load is concentrated directly above the center on the surface by the P_d load stream in comparison to the peak value found in Fig. 2(a). To avoid both problems of the maximum energy concentration occurring before the target time and a localized high surface load, we may attempt to control the system to achieve the objective, while using both cost functions.

Now, we choose weight factors w_1 and w_2 as 0.21 and 0.6, respectively, so that the objective has been satisfied by applying a surface force as small as possible with a relatively small system disturbance elsewhere. Figures 6(a) and 6(b) show the corresponding optimal surface normal load and its energy density contour plots inside the system, respectively. As expected, the optimal surface load lies somewhere between Figs. 2(a) and 5(a). Also, we notice that there is no high-energy concentration larger than the target value before the target time and no heavy compressional load occurs at the center of the surface, while the energy yield at the target is 23%. Thus, with both cost functions, an optimized balance is struck between the three competing factors of (i) reaching the target goal, (ii) yielding minimal system disturbance, and (iii) achieving minimal surface loading.

B. Control without a positive load constraint

When we remove the positive constraint from the optimal surface load conditions, the role of the cost function for the total surface force will decrease relatively due to the fact that we may exert smaller positive and negative load values instead of large positive ones to transmit the energy into the system efficiently. Figures 7(a) and 7(b) show the optimal surface normal load and its corresponding energy density contour plots for the case $w_1=0.0$ and $w_2=1.0$, so that the acoustic energy has been focused into the target volume only by applying minimum surface force. By comparison with Fig. 2(a), it is seen that the magnitude of the optimal surface load is decreased having both positive and negative values especially for the P_s load stream. Also, we notice that the P_d stream has a significant load value even at radii far away from the surface center. Figure 8 shows the contour plot of Fig. 7(a), the predicted load stream r versus t curve at velocities v_d and v_s, and the additional line corresponding to the shear wave velocity c_s. It is seen that the optimal surface load stream P_d and P_s shrink to the center with the velocity v_d and v_s, respectively, and the extrapolation of the earlier P_s load stream moving with the shear wave velocity meets the maximum values of the P_d load stream. Thus, the role of P_s stream can be interpreted as (1) producing a concentric surface wave at an early state as well as (2) directly feeding the acoustic energy into the half space as bulk motion to be transmitted to a focus in the target volume. Also, the stream P_d appears to play a role of feeding energy into the half space through compressional action by driving down the surface motion created by the P_s stream to the target volume.

When the load is moving with the shear wave velocity, the surface waves arising at different times will propagate with a common front. This front moves together with the leading edge of the load. As a result, the energy transmitted by the surface waves accumulates in the vicinity of the front of the load.[29] In order to analyze surface wave effects, the radial (u_r) and vertical (u_z) surface displacements due to the optimal surface normal load of Fig. 7(a) and their contour plots with the additional line

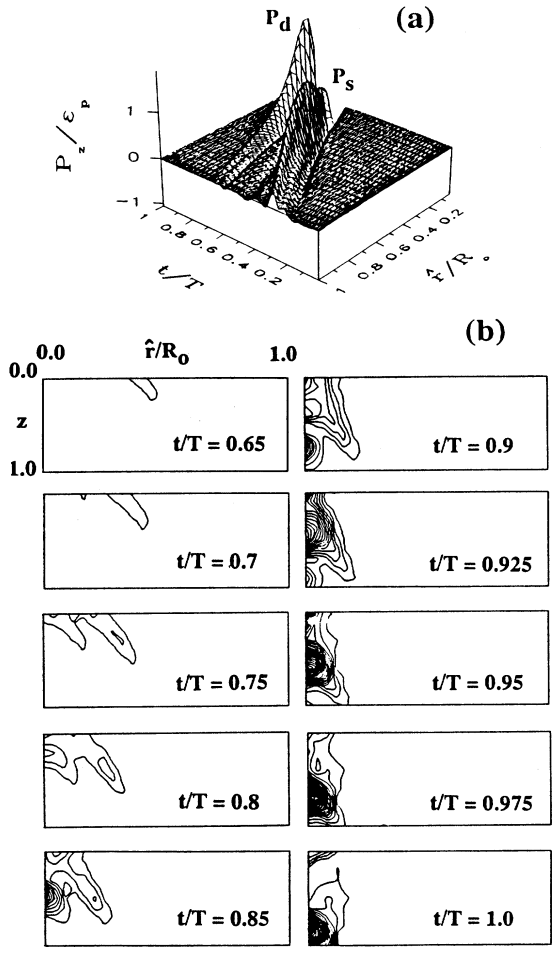

FIG. 7. (a) The optimal surface normal load without positive constraint and (b) the corresponding time sequence of optimally controlled energy density contour maps inside the Al alloy for $w_1=0.0$ and $w_2=1.0$. The contour interval is $\Delta\epsilon/\epsilon_p=0.1$, and the target time is $t/T=1$. Note that by applying only minimal surface force most of focused acoustic energy is generated through compressional action by driving down the surface motion created by the P_s load stream as well as directly transmitted shear wave motion.

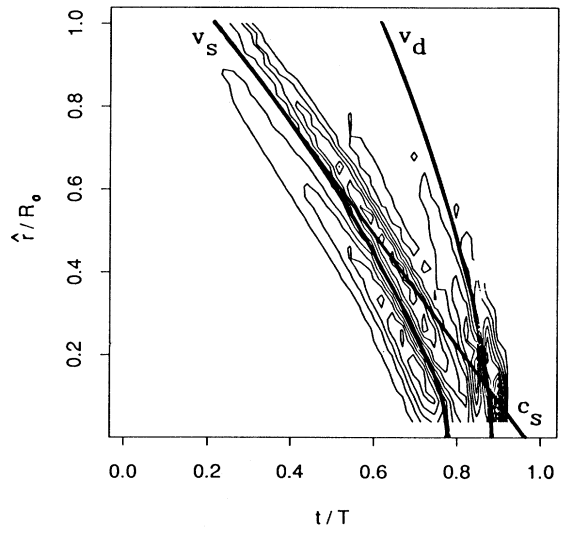

FIG. 8. The contour plot of the optimal surface load without positive constraint in Fig. 7(a), and the predicted load r vs t relations, which transmit the waves to the target center at the target time with the velocity c_d and c_s. The corresponding velocities v_d and v_s are obtained by the respective slope dr/dt. c_s labels the r vs t plot associated with the shear wave velocity. Note that the extrapolation of the earlier P_s load stream with velocity c_s meets the maximum value of the P_d load stream. It is evident that the surface motion created by the P_s load stream is converted by the P_d load stream into a bulk wave to better achieve the objective.

corresponding to the shear wave velocity are shown in Fig. 9. It is seen that the vertical surface displacements due to the P_s load stream shrink to the center of the surface associated with the shear wave velocity c_s and have a large upward (negative value) displacement at $t/T \sim 0.9$ and are changed to downward (positive value) displacements by the P_d load stream. The radial surface displacement has a dominant outward (positive value) motion moving to the center with the shear wave velocity until $t/T \sim 0.9$ when its amplitude is decreased by the P_d load stream. The load P_s also pushes a small inward (negative value) radial displacement ahead of its motion. The accumulated surface motions are aided in their transmission to the target volume by the load stream P_d at longitudinal velocity c_d. This effect can be easily seen from the energy contour plots in Fig. 7(b) for times greater than $t/T \sim 0.9$.

From the above facts, apparently the most efficient way of achieving subsurface energy focusing with a minimal surface force is to generate a concentric surface wave and eventually transmit it to the target by a P_d compressional load instead of only transmitting shear wave motion directly to the target volume by the P_s load alone. Figure 7(b) shows that at the target time, most of acoustic energy is focused in the target volume without any high-energy concentration occurring before the target time. However, the yield of the energy focusing processes is only 27%, but this is still twice as large as the analogous case in Fig. 2, where a positive constraint was applied.

To increase the yield of the energy focusing further, we studied the case with $w_1 = 0.15$ and $w_2 = 0.0$, so that the acoustic energy will be focused only with minimal system disturbance. The corresponding optimal surface load and energy density contour plots inside the medium are presented in Figs. 10(a) and 10(b), respectively. Similarly with comparison of the positive constraint cases of Figs. 2(a) and 5(a), the magnitude of P_d load stream is increased from Fig. 7(a), so that most of the acoustic energy is transmitted through the shortest path to the target by the P_d compressional load stream. The objective is satisfied at the target time efficiently with 68% of input energy from the surface being focused into the target volume at the target time. However, the P_d load is moderately high and a surface high-energy density region appears directly over the target.

As a final case, in order to achieve the objective efficiently without the remaining surface energy localization, we chose weight factors w_1 and w_2 as 0.07 and 0.6, respectively. Figures 11(a) and 11(b) show the corresponding optimal surface normal loads and the time se-

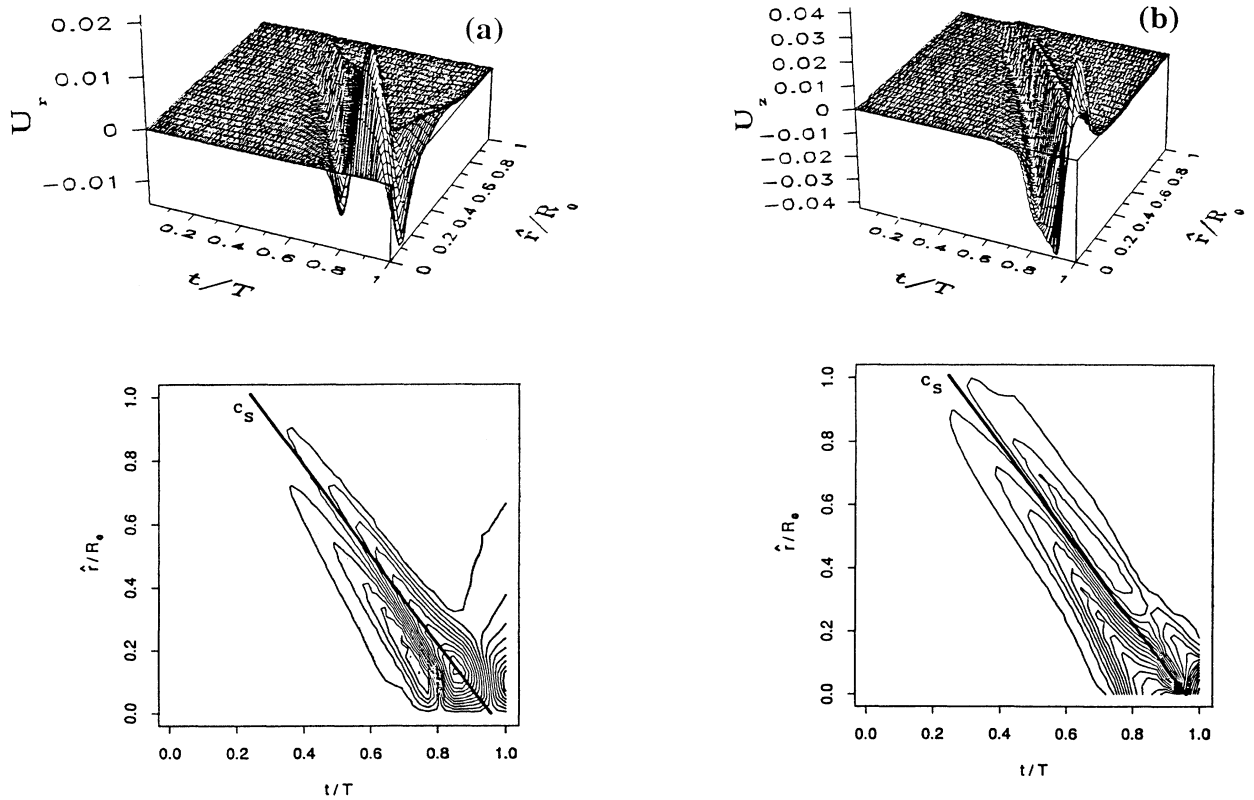

FIG. 9. The radial (u_r) and vertical (u_z) displacements due to the optimal surface normal load in Fig. 7(a) and their contour plots with the additional line corresponding to the shear wave velocity c_s. It is evident that surface motions due to the earlier P_s load stream shrink to the center of the surface with velocity c_s and are eventually transmitted to the target by the P_d load stream.

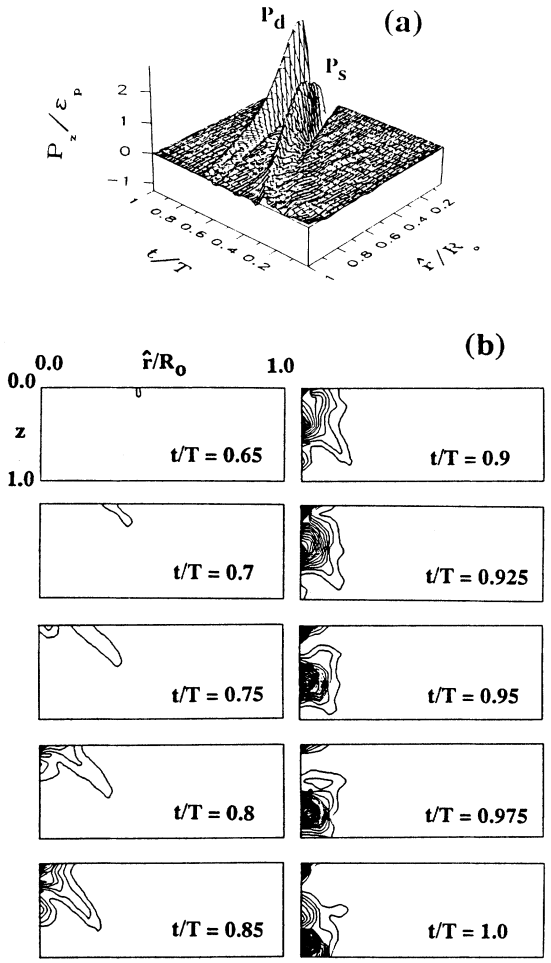

FIG. 10. Same as Fig. 7 except for $w_1=0.15$ and $w_2=0.0$. The contour interval is 0.1. Note that with only the minimum system disturbance cost, most of focused acoustic energy is generated by the longitudinal motions due to the highly concentrated surface load near the center of the surface.

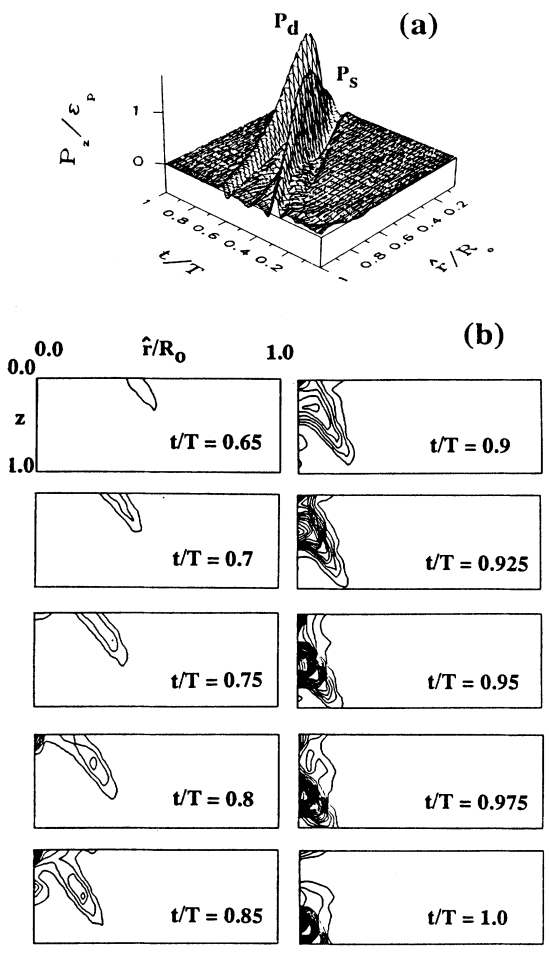

FIG. 11. Same as Fig. 7 except for $w_1=0.07$ and $w_2=0.6$. The contour interval is 0.1. Note that by applying a surface force as small as possible with relatively small system disturbance, the objective is achieved by the cooperation between those loads in order to enhance the energy efficiency with moderate surface force.

quence of the optimally controlled energy density contour plots inside the medium, respectively. It is seen that the optimal surface load has the same magnitude of the P_d load stream as Fig. 7a; however, the P_s load is now larger. As a result the cooperation between these loads is enhanced to produce an energy focusing efficiently of 42%. Thus, we have shown that with reasonable choices for the weight factors of the cost functions, subsurface acoustic-energy focusing may be achieved efficiently with relatively minimal surface force and simultaneously minimal system disturbance.

V. CONCLUSION

In this work optimal-control theory has been applied to design optimal dynamic normal loading of a homogeneous elastic solid for interior acoustic-energy focusing in a local target volume by applying a balanced minimum of surface forces and the smallest system disturbance. It is seen that the optimal dynamic surface loads, which lead to successfully achieved objectives with very high yield, are not simple intuitive structures. Although some intuition into the operative physical processes could be gained with hindsight, the necessary subtleties arise due to the acoustic-wave interference nature of the control process. The optimal surface loads need to be carefully tailored in order to increase the controlled efficiency of the process by the proper contribution of longitudinal, shear, and surface waves. Thus without consideration of tailored coherence, one would at most expect only a very small percentage of input energy to result in the target volume. In contrast, our optimal designs achieved up to 65% of the energy in the target. Also, in comparison with a scalar control field alone, the acoustic vector field has much greater ability for achieving the objective.

The work presented here can be extended to other types of objectives involving displacements, tractions, and/or strains either in the solid body or on one of its

bounding surfaces. The adoption of new appropriate cost functions and the choice of the weight factors gives the flexibility to take into account practical constraints. Given the acoustic-wave velocities, it may be possible to design a constrained optimal surface load having a chosen functional form with a set of parameters to be determined. For applications such as interior heating, melting, annealing, bonding dissimilar materials, and stopping crack propagation, a coupled thermoelastic optimal-control problem is underway in which heat transfer and elastodynamics are treated in a coupled way. The presence of solid defects may also be included to produce a stochastic control problem. Robustness demands can be included in the design process to assure that the results are minimally sensitive to system uncertainties or errors in load generation. The work in this area is only a beginning, but the results are promising for practical applications.

ACKNOWLEDGMENTS

The authors acknowledge support for this work from the Office of Naval Research. We also thank R. W. Ziolkowski for several helpful comments and drawing our attention to a related unpublished manuscript.[30]

APPENDIX: GREEN'S FUNCTION FOR A RING LOAD

An elastic half space occupying $z \geq 0$ of cylindrical coordinates (r,θ,z) is subjected to a ring load $(1/2\pi r)\delta(r-a)H(t)$ normal to the surface $z=0$, where $H(t)$ is the Heaviside unit step function. Since the load and the medium possesses axial symmetry with respect to the z axis, the displacement field $\mathbf{u}$ will also be axisymmetric. Therefore, of the three components (u_r,u_θ,u_z) of the displacement field, u_θ vanishes, and u_r and u_z are given in terms of the Helmholtz potential ϕ and ψ by

$$u_r=\frac{\partial\phi}{\partial r}-\frac{\partial\psi}{\partial z},\quad u_z=\frac{\partial\phi}{\partial z}+\frac{1}{r}\frac{\partial(r\psi)}{\partial r}\ . \tag{A1}$$

Here we write ψ rather than ψ_θ because for axially symmetric motion the vector potential ψ only has a component ψ_θ. The two potentials satisfy the wave equations,

$$\nabla^2\phi=\frac{1}{c_d^2}\frac{\partial^2\phi}{\partial t^2}\ ,\quad \nabla^2\psi-\frac{\psi}{r^2}=\frac{1}{c_s^2}\frac{\partial^2\psi}{\partial t^2}\ , \tag{A2}$$

where the constants c_d and c_s correspond to the longitudinal and shear wave velocity, respectively.

The resultant stresses σ_{zz} and σ_{zr} can be related to the displacements by

$$\sigma_{zz}=\lambda\left[\frac{\partial u_r}{\partial r}+\frac{u_r}{r}+\frac{\partial u_z}{\partial z}\right]+2\mu\frac{\partial u_z}{\partial z}\ , \tag{A3}$$

$$\sigma_{zr}=\mu\left[\frac{\partial u_r}{\partial z}+\frac{\partial u_z}{\partial r}\right]\ . \tag{A4}$$

The boundary condition for the ring load takes the form

$$\sigma_{zz}(r,0,t)=\frac{-1}{2\pi r}\delta(r-a)H(t),\quad \sigma_{zr}=0\ , \tag{A5}$$

and the initial conditions appear as

$$\phi(r,z,0)=\dot\phi(r,z,0)=\psi(r,z,0)=\dot\psi(r,z,0)=0\ . \tag{A6}$$

Solutions of the wave equation Eq. (A2), which satisfy the boundary and initial conditions may be calculated by using Laplace and Hankel transformations and give the Laplace-transformed displacements as

$$\bar u_{j\alpha}(r,z,p)=\int_0^\infty M_{j\alpha}(k,p)J_\beta(kr)J_0(ka)e^{-n_\alpha z}k\,dk\ , \tag{A7}$$

for $\alpha=d,s$ where $\beta=0$ if $j=z$ and $\beta=1$ if $j=r$, and

$$\begin{aligned} &M_{rd}(k,p)=kn_0/N,\quad M_{rs}(k,p)=-2kn_dn_s/N\ ,\\ &M_{zd}(k,p)=n_dn_0/N,\quad M_{zs}(k,p)=-2k^2n_d/N\ , \end{aligned} \tag{A8}$$

$$\begin{aligned} &n_d=(k^2+p^2/c_d^2)^{1/2},\quad n_s=(k^2+p^2/c_s^2)^{1/2}\ ,\\ &n_0=(2k^2+p^2/c_s^2),\quad N=2\pi\mu p(n_0^2-4k^2n_dn_s)\ . \end{aligned} \tag{A9}$$

From the well-known relations for Bessel functions,

$$\begin{aligned} &J_0(kr)J_0(ka)=\frac{1}{2\pi}\int_{-\pi}^{\pi}J_0(kR)d\varphi\ ,\\ &J_1(kr)J_0(ka)=\frac{1}{2\pi}\int_{-\pi}^{\pi}J_1(kR)\frac{r-a\cos\varphi}{R}d\varphi\ , \end{aligned} \tag{A10}$$

where

$$R=(a^2+r^2-2ar\cos\varphi)^{1/2}\ . \tag{A11}$$

The Laplace transformed displacement can be rewritten using Cagniard's method as

$$\bar u_{j\alpha}(r,z,p)=\frac{1}{4\pi}\int_{-\pi}^{\pi}d\varphi\,f_j(r,\varphi)\int_0^\infty\int_{-\infty}^{\infty}K_{j\alpha}(q,\omega)e^{-(p/c_d)(m_\alpha z-iqR)}dq\,d\omega\ , \tag{A12}$$

where

$$\begin{aligned} &K_{rd}(q,\omega)=-iqm_0/L,\quad K_{rs}(q,\omega)=2iqm_dm_s/L\ ,\\ &K_{zd}(q,\omega)=m_dm_0/L,\quad K_{zs}(q,\omega)=-2m_d(q^2+\omega^2)/L\ , \end{aligned} \tag{A13}$$

$$\begin{aligned} &m_d=(q^2+\omega^2+1)^{1/2},\quad m_s=(q^2+\omega^2+l^2)^{1/2}\ ,\\ &m_0=(2q^2+2\omega^2+l^2),\quad L=\pi^2c_d\mu[m_0^2-4(q^2+\omega^2)m_dm_s]\ ,\\ &f_r=\frac{r-a\cos\varphi}{R},\quad f_z=1,\quad l=\frac{c_d}{c_s}\ . \end{aligned} \tag{A14}$$

To evaluate Eq. (A12) by performing a contour integration in a complex q plane, we follow the same procedure used by Gakenheimer.[22] After inverting the Laplace transform, one finds the longitudinal motion as

$$u_{jd}(r,z,t)=\frac{1}{2\pi}\int_{-\pi}^{\pi}d\varphi\, f_j(r,\varphi)H(\tau-1)\int_0^{T_d}\mathrm{Re}\left[K_{jd}(q_d,\omega)\frac{dq_d}{dt}\right]d\omega\ , \tag{A15}$$

where

$$\begin{aligned} &q_d=(\tau^2-\tau_{\omega d}^2)^{1/2}z/\rho+i\tau R/\rho,\quad \rho^2=z^2+R^2\ ,\\ &T_d^2=\tau^2-1,\quad \tau=c_d t/\rho,\quad \tau_{\omega d}^2=\omega^2+1\ . \end{aligned} \tag{A16}$$

Similarly, the equivoluminal motion becomes

$$\begin{aligned} u_{js}(r,z,t)=\frac{1}{2\pi}\int_{-\pi}^{\pi}d\varphi\, f_j(r,\varphi)\Bigg[&H(\tau-l)\int_0^{T_s}\mathrm{Re}\left[K_{js}(q_s,\omega)\frac{dq_s}{dt}\right]d\omega\\ &+H(\tau-\tau_{sd})H(\tau'_{sd}-\tau)H(l-\rho/R)\int_{A_{sd}}^{T_{sd}}\mathrm{Re}\left[K_{js}(q_{sd},\omega)\frac{dq_{sd}}{dt}\right]d\omega\Bigg]\ , \end{aligned} \tag{A17}$$

where

$$\begin{aligned} &q_s=(\tau^2-\tau_{\omega s}^2)^{1/2}z/\rho+i\tau R/\rho,\quad q_{sd}=-i(\tau_{\omega s}^2-\tau^2)^{1/2}z/\rho+i\tau R/\rho\ ,\\ &T_s^2=\tau^2-l,\quad T_{sd}^2=[(\tau-\tau_{sd})\rho/R+1]^2-1\ ,\\ &\tau_{\omega s}^2=\omega^2+l^2,\quad \tau_{sd}=R/\rho+z(l^2-1)^{1/2}/\rho,\quad \tau'_{sd}=(l^2-1)^{1/2}\rho/z\ ,\\ &A_{sd}=\begin{cases}0, & \text{for } \tau_{sd}<\tau<l\\ T_s, & \text{for } l<\tau<\tau'_{sd}\ .\end{cases} \end{aligned} \tag{A18}$$

The second term in Eq. (A17) represents the equivoluminal motion behind the head wave front at $\tau=\tau_{sd}$ for $\rho/R<l$, which is generated by the surface interaction of the longitudinal wave front at $\tau=1$.

All of the Green's functions of this work involve an integral that must be evaluated by numerical methods. The integrands contain a singularity at each wave front. Although it is an integrable singularity, it may lead to numerical problems. With a simple transformation of variables one can avoid this problem. For example, the substitution $\omega=(\tau^2-1)^{1/2}-\eta^2$ in Eq. (A15) gives[31]

$$u_{jd}(r,z,t)=\frac{c_d}{\pi\rho}\int_{-\pi}^{\pi}d\varphi\, f_j(r,\varphi)H(\tau-1)\int_0^{(\tau^2-1)^{1/4}}\mathrm{Re}[K_{jd}(q_d,\omega)Q_d]d\eta\ , \tag{A15'}$$

which no longer contains a singularity and where

$$Q_d=\tau[2(\tau^2-1)^{1/2}-\eta^2]^{-1/2}z/\rho+i\eta R/\rho\ . \tag{A16'}$$

Then, the integrals can be readily evaluated with standard quadrature methods. The Green's function for the δ-time function ring-load can be written by differentiation with respect to time as

$$G_{R,jz}(r,z,t;a)=\frac{\partial}{\partial t}(u_{jd}+u_{js})\ . \tag{A19}$$

It is also apparent from the form of the Green's functions that after the integral has been evaluated numerically it must be differentiated with respect to time. However, in most cases the numerical differentiation of the Green's function can be avoided using the convolution properties.

---

*Department of Applied Science, Hong-Ik University, Mapo-ku, Seoul 121, Korea.

[1]See, e.g., D. G. Luenberger, *Introduction to Dynamic System, Theory, Models, and Applications* (Wiley, New York, 1979).
[2]S. Shi, A. Woody, and H. Rabitz, J. Chem. Phys. **88**, 6870 (1988).
[3]J. N. Brittingham, J. Appl. Phys. **54**, 1179 (1983).
[4]R. W. Ziolkowski, Phys. Rev. A **39**, 2005 (1989).
[5]R. W. Ziolkowski, D. K. Lewis, and B. D. Cook, Phys. Rev. Lett. **62**, 147 (1989).
[6]P. Hillion, J. Appl. Phys. **60**, 2981 (1986); J. Math. Phys. **28**, 1743 (1987).
[7]T. T. Wu, J. Appl. Phys. **57**, 2370 (1985); T. T. Wu, R. W. P. King, and H.-M. Shen, J. Appl. Phys. **62**, 4036 (1987).
[8]J. Durnin, J. Opt. Soc. Am. A **4**, 651 (1987); J. Durnin, J. J. Miceli, Jr., and J. H. Eberly, Phys. Rev. Lett. **58**, 1499 (1987).

[9]H. E. Moses, J. Math. Phys. **25**, 1905 (1984); H. E. Moses and R. T. Prosser, IEEE Trans. Antennas Propag. **AP-34**, 188 (1986).

[10]E. Heyman and L. P. Felsen, IEEE Trans. Antennas Propag. **AP-34**, 1062 (1986); E. Heyman and B. Z. Steinberg, J. Opt. Soc. Am. A **4**, 473 (1987); E. Heyman, B. Z. Steinberg, and L. P. Felsen, *ibid.* **4**, 2081 (1987).

[11]See, e.g., Y. H. Pao, ASME J. Appl. Mech. **50**, 1152 (1983).

[12]H. W. Jones and H. W. Kwan, Ultrasonics **23**, 63 (1985).

[13]C. B. Scruby, R. J. Dewhurst, D. A. Hutchins, and S. B. Palmer, J. Appl. Phys. **51**, 6210 (1980); R. J. Dewhurst, D. A. Hutchins, S. B. Palmer, and C. B. Scruby, Appl. Phys. Lett. **38**, 677 (1981); J. Appl. Phys. **53**, 4064 (1982).

[14]R. M. White, J. Appl. Phys. **34**, 3559 (1963); J. E. Sinclair, J. Phys. D **12**, 1309 (1979); L. R. F. Rose, J. Acoust. Soc. Am. **75**, 723 (1984).

[15]R. R. Boade and O. L. Burchett, J. Appl. Phys. **47**, 3412 (1976); L. J. Balk, Can. J. Phys. **64**, 1238 (1986).

[16]A. J. A. Bruinsma and J. A. Vogel, Appl. Opt. **27**, 4690 (1988).

[17]F. R. Breckenridge, C. E. Tschiegg, and M. Greenspan, J. Acoust. Soc. Am. **57**, 626 (1975); N. N. Hsu and S. C. Hardy, in *Elastic Waves and Non-Destructive Testing*, edited by Y. H. Pao (ASME, New York, 1978), pp. 85–106; for a review, see, e.g., R. B. Thompson, ASME J. Appl. Mech. **50**, 1191 (1983).

[18]For a review, see e.g., D. A. Hutchins, Can. J. Phys. **64**, 1247 (1986).

[19]C. A. Brebbia, *The Boundary Element Method for Engineers* (Pentech, London, 1978).

[20]C. A. Brebbia and J. J. Connor, *Fundamentals of Finite Elements Techniques for Structural Engineers* (Butterworths, London, 1973).

[21]A. E. Bryson, Jr. and Yu-Chi Ho, *Applied Optimal Control* (Wiley, New York, 1975).

[22]D. C. Gakenheimer, ASME J. Appl. Mech. **38**, 99 (1971).

[23]D. M. Cole, D. D. Kosloff, and J. B. Minster, Bull. Seismol. Soc. Am. **68**, 1331 (1978).

[24]R. A. Meric, Int. J. Eng. Sci. **23**, 1101 (1985).

[25]See, e.g., P. M. Morse and F. Feshbach, *Methods of Theoretical Physics* (McGraw-Hill, New York, 1953).

[26]M. J. D. Powell, Math. Prog. **12**, 241 (1977).

[27]D. I. Rosen, J. Mitteldorf, G. Kothandaraman, A. N. Pirri, and E. R. Pugh, J. Appl. Phys. **53**, 3190 (1982).

[28]G. F. Miller and H. Pursey, Proc. R. Soc. London, Ser. A **223**, 521 (1954); **233**, 55 (1955).

[29]R. V. Gol'dshtein, J. Appl. Math. Mech. **29**, 516 (1965).

[30]J. E. Hermandez, R. W. Ziolkowski, and S. R. Parker (unpublished).

[31]L. R. Johnson, Geophys. J. R. Astron. Soc. **37**, 99 (1974).